Earth, Planets and Space

FULL PAPER Open Access

The Mie representation for Mercury's magnetic field

S. Toepfer[1*], Y. Narita[2,3], K. -H. Glassmeier[3], D. Heyner[3], P. Kolhey[3], U. Motschmann[1,4] and B. Langlais[5]

Abstract

The parameterization of the magnetospheric field contribution, generated by currents flowing in the magnetosphere is of major importance for the analysis of Mercury's internal magnetic field. Using a combination of the Gauss and the Mie representation (toroidal–poloidal decomposition) for the parameterization of the magnetic field enables the analysis of magnetic field data measured in current carrying regions in the vicinity of Mercury. In view of the BepiColombo mission, the magnetic field resulting from the plasma interaction of Mercury with the solar wind is simulated with a hybrid simulation code and the internal Gauss coefficients for the dipole, quadrupole and octupole field are reconstructed from the data, evaluated along the prospective trajectories of the Mercury Planetary Orbiter (MPO) using Capon's method. Especially, it turns out that a high-precision determination of Mercury's octupole field is expectable from the future analysis of the magnetic field data measured by the magnetometer on board MPO. Furthermore, magnetic field data of the MESSENGER mission are analyzed and the reconstructed internal Gauss coefficients are in reasonable agreement with the results from more conventional methods such as the least-square fit.

Keywords: Mie representation, Poloidal and toroidal magnetic fields, Thin shell approximation, Gauss representation, Capon's method

Introduction

Characterization of Mercury's internal magnetic field is one of the primary goals of the BepiColombo mission (Benkhoff et al. 2010). The magnetic field in the vicinity of Mercury is composed of internal and external parts. The internal field originates in the dynamo-generated field, crustal remanent field and induction field, which are mainly dominated by the dipole, quadrupole and octupole field. The external field originates from currents flowing in the magnetosphere. For a clear separation of the internal magnetic field from the external field, each part of the magnetic field has to be modeled properly. Especially the parameterization of the external parts is of major importance since these parts contribute a significant amount to the total field within Mercury's magnetosphere (Anderson et al. 2011).

Above the planetary surface, the internal part of the field is a current-free magnetic field which can be parameterized by the Gauss representation (Gauß 1839; Glassmeier and Tsurutani 2014). When only data in source-free regions without currents are analyzed, the Gauss representation also yields a parametrization for the external parts of the field (Olsen et al. 2010). But in the vicinity of Mercury significant currents are expected (Anderson et al. 2011, eg); and therefore, the Gauss representation is insufficient due to the current-generated magnetic field outside the planet. In this paper, we construct a parametric Mercury magnetic field model by extending the Gauss representation to the Gauss–Mie representation.

Previous studies parameterized the external parts by making use of a global magnetospheric model, such as the paraboloid model for Mercury's magnetosphere

*Correspondence: s.toepfer@tu-braunschweig.de
[1] Institut für Theoretische Physik, Technische Universität Braunschweig, Mendelssohnstraße 3, 38106 Braunschweig, Germany
Full list of author information is available at the end of the article

(Alexeev et al. 2008), that has successfully been applied to the analysis of Mercury's internal and external magnetic field (Alexeev et al. 2010; Johnson et al. 2021), as well as the modified Tsyganenko model (Korth et al. 2004). As an alternative for these models the Mie representation is useful for decomposing the magnetic field in current carrying regions in the vicinity of Mercury (Backus 1986; Olsen 1997; Olsen et al. 2010).

The Mie representation, also known as toroidal-poloidal decomposition, is based on the solenoidality of the magnetic field and enables to decompose the field into its toroidal and poloidal parts (Backus 1986; Backus et al. 1996; Kazantsev and Kardakov 2019). This representation has successfully been applied to several problems in space plasma physics, especially for the analysis of the Earth's magnetosphere. For example, Engels and Olsen (1999) used the Mie representation for calculating the magnetic effect caused by a three dimensional current density model. Olsen (1997) applied the Mie representation to reconstruct ionospheric F-currents in the Earth's magnetosphere from MAGSAT data. Furthermore, Bayer et al. (2001) introduced the wavelet Mie representation of the magnetic field to calculate current densities from MAGSAT and CHAMP data. This approach has been expanded on the modeling of the Earth's magnetic field in terms of vector kernel functions (Mayer and Maier 2006). Kosik (1984) constructed a model for the Earth's magnetosphere based on the Mie representation.

In this work, the magnetic field in the vicinity of Mercury is parameterized by a combination of the Gauss and the Mie representation (hereafter, Gauss–Mie representation), based on the works of Backus (1986), Backus et al. (1996) and Olsen (1997), for analyzing Mercury's internal magnetic field. The desired internal Gauss coefficients for the dipole, quadrupole and octupole field are estimated with Capon's method (Capon 1969). The Capon method serves as a powerful inversion method for linear inverse problems and was used by, e.g., Motschmann et al. (1996), Glassmeier et al. (2001), Narita et al. (2006) and Narita (2012) to evaluate spatial spectra of space plasma waves. As shown by Toepfer et al. (2020a) the Capon method can also be used in a generalized way to compare actual measurements with theoretical models. Here, we expand on this method. First of all, the mathematical foundations of the Mie representation, as derived by Backus (1986) and Backus et al. (1996) are revisited. Afterwards, the resulting thin shell approximation is applied to simulated magnetic field data, that are evaluated along the future data points of the Mercury Planetary Orbiter (MPO). This enables the judgement of the expectable inversion results from the data of the magnetometer (Glassmeier et al. 2010; Heyner et al. 2020) on board MPO. Finally, the model is applied to MESSENGER data and the reconstructed Gauss coefficients are compared with the results of former works by Anderson et al. (2012), Thébault et al. (2018) and Wardinski et al. (2019).

The Mie representation

The solenoidality of the magnetic field $\underline{B}$ guarantees the existence of a vector potential $\underline{A}$, so that

$$\underline{B} = \partial_{\underline{x}} \times \underline{A} \tag{1}$$

holds, where $\partial_{\underline{x}}$ is the spatial derivative. Using spherical coordinates with radius $r \in [0, \infty)$, longitude $\lambda \in [0, 2\pi]$ and co-latitude angle $\theta \in [0, \pi]$ the vector potential can be seperated into its component $\Psi_T \underline{r}$ parallel to $\underline{r} = r\,\underline{e}_r$, where $\underline{e}_r$ is the unit vector in radial direction, and its components $\underline{F} \times \underline{r}$ perpendicular to $\underline{r}$, yielding

$$\underline{A} = \Psi_T \underline{r} + \underline{F} \times \underline{r} + \partial_{\underline{x}} \varphi \tag{2}$$

with the scalar functions Ψ_T and φ as well as a vector field $\underline{F}$ (Jacobs 1987; Krause and Rädler 1980). Because of $\partial_{\underline{x}} \times \partial_{\underline{x}} \varphi = 0$, the function φ can be chosen properly so that $\partial_{\underline{x}} \times \underline{F} = 0$ holds, and therefore

$$\underline{F} = \partial_{\underline{x}} \Psi_P \tag{3}$$

with a scalar function Ψ_P without changing the magnetic field (Jacobs 1987; Krause and Rädler 1980). The vector potential results in

$$\underline{A} = \Psi_T \underline{r} + \partial_{\underline{x}} \Psi_P \times \underline{r} \tag{4}$$

$$= \Psi_T \underline{r} + \partial_{\underline{x}} \times (\Psi_P \underline{r}). \tag{5}$$

Substituting $\underline{A}$ into Eq. (1) delivers

$$\underline{B} = \partial_{\underline{x}} \times (\Psi_T \underline{r}) + \partial_{\underline{x}} \times \left[\partial_{\underline{x}} \times (\Psi_P \underline{r})\right], \tag{6}$$

which is called the Mie representation of the magnetic field (Backus 1986; Backus et al. 1996).

The first term on the right hand side in Eq. (6)

$$\underline{B}_T = \partial_{\underline{x}} \times (\Psi_T \underline{r}) \tag{7}$$

is the toroidal part of the field and the second term

$$\underline{B}_P = \partial_{\underline{x}} \times \left[\partial_{\underline{x}} \times (\Psi_P \underline{r})\right] \tag{8}$$

is the poloidal part of $\underline{B}$.

From the definition of $\underline{B}_T$ and $\underline{B}_P$ it is clear that $\underline{B}_T$ is perpendicular to $\underline{B}_P$ and also perpendicular to $\underline{r}$. Therefore, the toroidal part of the field does not have a radial component. Furthermore, poloidal magnetic fields are generated by toroidal currents and vice versa:

$$\partial_{\underline{x}} \times \underline{B}_T = \partial_{\underline{x}} \times \left[\partial_{\underline{x}} \times (\underline{r} \Psi_T)\right] \tag{9}$$

is a poloidal vector and

$$\partial_{\underline{x}} \times \underline{B}_P = \partial_{\underline{x}} \times \left[\partial_{\underline{x}} \times \left[\partial_{\underline{x}} \times (\underline{r}\Psi_P)\right]\right] = \partial_{\underline{x}} \times \left[\left(-\partial^2_{\underline{x}}\Psi_P\right)\underline{r}\right] \tag{10}$$

is a toroidal vector.

In curl-free regions where especially the poloidal current density $\underline{j}_P$ vanishes, Ampère's law reads as follows:

$$\mu_0 \underline{j}_P = \partial_{\underline{x}} \times \left[\partial_{\underline{x}} \times (\Psi_T \underline{r})\right] = -\underline{r}\partial^2_{\underline{x}}\Psi_T + \partial_{\underline{x}}\partial_r(r\Psi_T) = 0 \tag{11}$$

or equivalently

$$\partial_{\underline{x}}\partial_r(r\Psi_T) = \underline{r}\partial^2_{\underline{x}}\Psi_T. \tag{12}$$

Therefore, the gradient of $\partial_r(r\Psi_T)$ has only a radial component, leaving us with

$$\partial_\lambda \Psi_T = 0 = \partial_\theta \Psi_T, \tag{13}$$

so that the function Ψ_T solely depends on the radial distance from the center ($\Psi_T = \Psi_T(r)$) and thus, the toroidal magnetic field vanishes

$$\underline{B}_T = \partial_{\underline{x}} \times (\Psi_T \underline{r}) = \left(\partial_{\underline{x}}\Psi_T\right) \times \underline{r} = \partial_r \Psi_T \underline{e}_r \times \underline{r} = 0. \tag{14}$$

On the other hand, when the toroidal current density vanishes

$$\mu_0 \underline{j}_T = \partial_{\underline{x}} \times \partial_{\underline{x}} \times \left[\partial_{\underline{x}} \times (\Psi_P \underline{r})\right] = \partial_{\underline{x}} \times \left[-r\left(\partial^2_{\underline{x}}\Psi_P\right)\underline{e}_r\right] \tag{15}$$

$$= \frac{1}{r\sin(\theta)}\partial_\varphi\left[-r\partial^2_{\underline{x}}\Psi_P\right]\underline{e}_\theta - \frac{1}{r}\partial_\theta\left[-r\partial^2_{\underline{x}}\Psi_P\right]\underline{e}_\varphi \tag{16}$$

$$= 0 \tag{17}$$

or equivalently

$$\partial_\varphi \partial^2_{\underline{x}}\Psi_P = 0 \tag{18}$$

and simulanously

$$\partial_\theta \partial^2_{\underline{x}}\Psi_P = 0 \tag{19}$$

the function $\partial^2_{\underline{x}}\Psi_P$ solely depends on the radius. Therefore, the poloidal field

$$\underline{B}_P = \partial_{\underline{x}} \times \left[\partial_{\underline{x}} \times (\Psi_P \underline{r})\right] = -\underline{r}\partial^2_{\underline{x}}\Psi_P + \partial_{\underline{x}}\partial_r(r\Psi_P) \neq 0 \tag{20}$$

in general remains finite in current-free regions.

Relation to the Gauss representation

When magnetic field data in curl-free regions (where $\partial_{\underline{x}} \times \underline{B} = 0$ holds) are analyzed, there exists a scalar potential Φ so that the magnetic field can be written as

$$\underline{B} = -\partial_{\underline{x}}\Phi = -\partial_r\Phi\,\underline{e}_r - \frac{1}{r}\partial_\theta\Phi\,\underline{e}_\theta - \frac{1}{r\sin(\theta)}\partial_\lambda\Phi\,\underline{e}_\lambda, \tag{21}$$

which is known as the Gauss representation of the magnetic field (Gauß 1839; Glassmeier and Tsurutani 2014). Simultanously, the Mie representation in due consideration that the toroidal magnetic field vanishes in curl-free regions is given by

$$\underline{B} = \partial_{\underline{x}} \times \left[\partial_{\underline{x}} \times (\Psi_P \underline{r})\right] \tag{22}$$

$$= \frac{1}{r\sin(\theta)}\left[-\partial_\theta(\sin(\theta)\partial_\theta\Psi_P) - \frac{1}{\sin(\theta)}\partial^2_\lambda\Psi_P\right]\underline{e}_r \tag{23}$$

$$+ \frac{1}{r}\partial_\theta\partial_r(r\Psi_P)\underline{e}_\theta + \frac{1}{r\sin(\theta)}\partial_\lambda\partial_r(r\Psi_P)\underline{e}_\lambda \tag{24}$$

Comparison of coefficients with Eq. (21) for $\underline{e}_\theta$ shows that

$$\frac{1}{r}\partial_r\partial_\theta(r\Psi_P) = -\frac{1}{r}\partial_\theta\Phi \tag{25}$$

and analogously for $\underline{e}_\lambda$

$$\frac{1}{r\sin(\theta)}\partial_r\partial_\lambda(r\Psi_P) = -\frac{1}{r\sin(\theta)}\partial_\lambda\Phi. \tag{26}$$

Consequently, when Ψ_P is known, the scalar potential is given by

$$\Phi = -\partial_r(r\Psi_P). \tag{27}$$

Comparison of the $\underline{e}_r$-coefficients delivers

$$\frac{1}{r\sin(\theta)}\left[\partial_\theta(\sin(\theta)\partial_\theta\Psi_P) + \frac{1}{\sin(\theta)}\partial^2_\lambda\Psi_P\right] = \partial_r\Phi \tag{28}$$

or equivalently

$$\partial^2_S\Psi_P = \frac{1}{r}\partial_r\Phi, \tag{29}$$

where

$$\partial^2_S = \frac{1}{r^2\sin(\theta)}\partial_\theta(\sin(\theta)\partial_\theta\,) + \frac{1}{r^2\sin^2(\theta)}\partial^2_\lambda \tag{30}$$

is the angular part of the Laplacian. For a given Φ, the function Ψ_P can be found by solving Eqs. (27, 29) simultanously.

As a consequence, the scalar function Ψ_P and the scalar potential Φ are equivalent in curl-free regions and the Mie representation transists into the Gauss representation. Thus, the Gauss representation can be understood as a special case of the Mie representation.

Parameterization of the magnetic field

Assuming that the conductivity of Mercury's mantle is negligibly small (like lunar regolith (Zharkova et al. 2020)), the planetary contribution to the field outside Mercury is purely poloidal. The currents flowing in the magnetosphere generate poloidal and toroidal magnetic fields that superpose with the curl-free planetary magnetic field. To be able to separate the planetary magnetic field out of the measured field and to parameterize it via the Gauss coefficients, a combined parametrization composed of the Mie and the Gauss representation (Gauss–Mie representation), which is based on the works of Backus (1986) and Olsen (1997) is necessary.

Suppose that the magnetic field in the vicinity of Mercury is measured within a spherical shell $S(a,c)$ with inner radius $a > R_{\mathrm{M}}$, where R_{M} indicates the radius of Mercury, outer radius c and mean radius $b = \frac{1}{2}(a+c)$ as displayed in Fig. 1. The shell can be constructed independently of the orbit's geometry by conceptually covering the orbit of the spacecraft. Furthermore, the shell may include current carrying regions. Although the Mie representation enables us to analyze those currents, we focus on the analysis of Mercury's internal magnetic field.

Due to the underlying geometry, the space around Mercury can be decomposed into three disjoint radial zones:

- points in the region $r < a$ below the shell
- points in the region $r > c$ above the shell
- points in the region $a \leq r \leq c$ inside the shell layer

Making use of the superposition principle the total magnetic field $\underline{B}$ measured inside the shell layer $(a \leq r \leq c)$ is a composition of the field $\underline{B}_{j\in[a,c]}$ generated by currents flowing inside the shell and the field $\underline{B}_{j\notin[a,c]}$ generated by currents flowing outside the shell. Again considering the underlying geometry, the second part can be divided into an internal part $\underline{B}^i$ resulting from currents flowing in the region $r < a$ and an external part $\underline{B}^e$ resulting from currents flowing in the region $r > c$, so that

$$\underline{B}_{j\notin[a,c]} = \underline{B}^i + \underline{B}^e. \tag{31}$$

As $\underline{B}^i$ and $\underline{B}^e$ have their sources beyond the shell they are purely poloidal and especially nonrotational within the shell. Thus, there exist scalar potentials Φ^i and Φ^e so that the field can be parameterized in the shell via the Gauss representation resulting in

$$\underline{B}^i = -\,\partial_{\underline{x}}\Phi^i \tag{32}$$

and

$$\underline{B}^e = -\,\partial_{\underline{x}}\Phi^e, \tag{33}$$

where the scalar potentials are given by (Gauß 1839; Glassmeier and Tsurutani 2014)

$$\Phi^i = R_{\mathrm{M}} \sum_{l=1}^{\infty}\sum_{m=0}^{l}\left(\frac{R_{\mathrm{M}}}{r}\right)^{l+1} \left[g_l^m\,\cos(m\lambda) + h_l^m\,\sin(m\lambda)\right] P_l^m(\cos(\theta)) \tag{34}$$

and

$$\Phi^e = R_{\mathrm{M}} \sum_{l=1}^{\infty}\sum_{m=0}^{l}\left(\frac{r}{R_{\mathrm{M}}}\right)^{l} \left[q_l^m\,\cos(m\lambda) + s_l^m\,\sin(m\lambda)\right] P_l^m(\cos(\theta)). \tag{35}$$

The expansion coefficients g_l^m and h_l^m are the internal Gauss coefficients, the coefficients q_l^m and s_l^m are the external Gauss coefficients and P_l^m are the Schmidt normalized Legendre polynomials of degree l and order m. Since Mercury's internal magnetic field is dominated by the internal dipole, quadrupole and octupole fields, the series expansions in Eqs. (34, 35) will be truncated at the degree $l = 3$ for the practical application.

It should be noted that the internal field $\underline{B}^i$ is canonically described in a Mercury-Body-Fixed co-rotating coordinate system (MBF), whereas the external field $\underline{B}^e$ is canonically described in a Mercury-Solar-Orbital system (MSO) with the x-axis orientated towards the sun, the z-axis orientated parallel to the rotation axis, i.e. antiparallel to the internal dipole moment, and the y-axis completes the right-handed system (Heyner et al. 2020). Let $\underline{x}_{\mathrm{MSO}} = \left(x_{\mathrm{MSO}}, y_{\mathrm{MSO}}, z_{\mathrm{MSO}}\right)^T$ define the MSO coordinate system and let $\underline{x}_{\mathrm{MBF}} = \left(x_{\mathrm{MBF}}, y_{\mathrm{MBF}}, z_{\mathrm{MBF}}\right)^T$ be the coordinates of the co-rotating MBF system. Then, the internal parts of the field are given by

$$\underline{B}^i(\underline{x}_{\mathrm{MBF}}) = -\partial_{\underline{x}_{\mathrm{MBF}}}\Phi^i(\underline{x}_{\mathrm{MBF}}) = \underline{\underline{H}}^i(\underline{x}_{\mathrm{MBF}})\,\underline{g}^i, \tag{36}$$

whereas the external parts are described in the MSO system, i.e.

$$\underline{B}^e(\underline{x}_{\mathrm{MSO}}) = -\partial_{\underline{x}_{\mathrm{MSO}}}\Phi^e(\underline{x}_{\mathrm{MSO}}) = \underline{\underline{H}}^e(\underline{x}_{\mathrm{MSO}})\,\underline{g}^e, \tag{37}$$

where the terms of the series expansion are arranged into the matrices $\underline{\underline{H}}^i$ and $\underline{\underline{H}}^e$ and the corresponding Gauss coefficients are summarized into the vectors $\underline{g}^i$ and $\underline{g}^e$.

The co-rotating MBF system can be transformed into the MSO system via

$$\underline{x}_{\mathrm{MSO}} = \underline{\underline{A}}\,\underline{x}_{\mathrm{MBF}}, \tag{38}$$

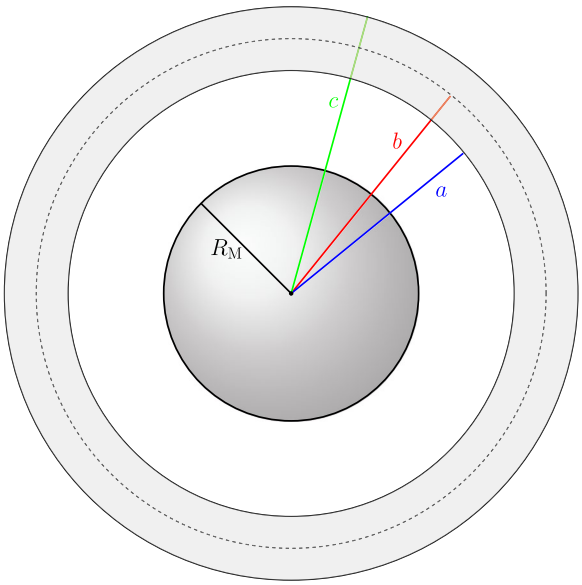

Fig. 1 Cross section of the spherical shell $S(a,c)$ with inner radius a, outer radius c and mean radius $b = (a+c)/2$. The inner sphere with radius R_M symbolizes Mercury

where $\underline{\underline{A}}$ describes a rotation matrix around the z-axis depending on the angular velocity of Mercury's self-rotation measured within the MSO system.

For the practical application it is convenient to describe both parts of the field in one coordinate system, for example the MSO system. The transformed data are given by

$$\underline{B}\left(\underline{x}_{\mathrm{MSO}}\right) = \underline{\underline{A}}\,\underline{B}^{i}\left(\underline{x}_{\mathrm{MBF}}\right) + \underline{B}^{e}\left(\underline{x}_{\mathrm{MSO}}\right) \tag{39}$$

$$= \underline{\underline{A}}\,\underline{\underline{H}}^{i}\left(\underline{x}_{\mathrm{MBF}}\right)\underline{g}^{i} + \underline{\underline{H}}^{e}\left(\underline{x}_{\mathrm{MSO}}\right)\underline{g}^{e} \tag{40}$$

in the MSO system.

Since for the first validation the model will be applied to simulated magentic field data, it is useful to match the coordinate system of the parametrization with the coordinate system of the simulation. Therefore, in the following all parts of the magnetic field are described in a Mercury-Body-Fixed anti-solar orientated coordinate system (MASO) with coordinates $\underline{x} = (x,y,z)^T$, where the x-axis is orientated towards the nightside of Mercury (away from the sun), the z-axis is orientated antiparallel to the internal dipole moment and the y-axis completes the right-handed system, so that

$$\underline{x} = \begin{bmatrix} -1 & 0 & 0 \\ 0 & -1 & 0 \\ 0 & 0 & 1 \end{bmatrix} \underline{x}_{\mathrm{MSO}}. \tag{41}$$

As already mentioned in the introduction ("Introduction" section) there is no current-free shell-like region around Mercury (Olsen et al. 2010). The currents flowing in the shell generate toroidal $\underline{B}_T^{sh}$ and poloidal $\underline{B}_P^{sh}$ magnetic fields which superpose with $\underline{B}^i$ and $\underline{B}^e$. Thus, the total measured field within the shell is composed of four parts given by

$$\underline{B} = \underline{B}_{\underline{j}\notin[a,c]} + \underline{B}_{\underline{j}\in[a,c]} = \underline{B}^i + \underline{B}^e + \underline{B}_T^{sh} + \underline{B}_P^{sh} \tag{42}$$

$$= -\partial_{\underline{x}}\Phi^i - \partial_{\underline{x}}\Phi^e + \partial_{\underline{x}} \times \left[\partial_{\underline{x}} \times \left(\underline{r}\Psi_P^{sh}\right)\right] + \partial_{\underline{x}} \times \left(\underline{r}\Psi_T^{sh}\right), \tag{43}$$

where each part of the field is described either by a scalar potential Φ^i, Φ^e or a scalar function Ψ_P^{sh}, Ψ_T^{sh}.

The scalar potentials Φ^i and Φ^e are already parameterized by the Gauss coefficients. In the following, a proper parameterization for the scalar functions Ψ_T^{sh} and Ψ_P^{sh} is required. Because of the underlying spherical geometry it is straightforward to expand the functions into spherical harmonics

$$\Psi_T^{sh} = \sum_{l=1}^{\infty}\sum_{m=0}^{l}\left[a_l^m(r)\,\cos(m\lambda) + b_l^m(r)\,\sin(m\lambda)\right]P_l^m(\cos(\theta)) \tag{44}$$

and

$$\Psi_P^{sh} = R_{\mathrm{M}}\sum_{l=1}^{\infty}\sum_{m=0}^{l} \left[c_l^m(r)\,\cos(m\lambda) + d_l^m(r)\,\sin(m\lambda)\right]P_l^m(\cos(\theta)), \tag{45}$$

where $a_l^m(r)$, $b_l^m(r)$, $c_l^m(r)$ and $d_l^m(r)$ are the expansion coefficients which in general depend on the radius r and again P_l^m are the Schmidt normalized Legendre polynomials. Since the toroidal and poloidal fields can be locally generated by currents flowing in the shell the radial dependences of the fields and the expansion coefficients, respectively, are unknown.

Series expansion of the coefficients

Since the exact radial dependence of the expansion coefficients $a_l^m(r)$ and $b_l^m(r)$ is unknown, it is useful to expand these functions into a Taylor series in the vicinity of the mean radius b of the shell. Within this series expansion it is advisable not to incorporate the effect of all components of the poloidal current density to the toroidal magnetic field at once. Here, we first concentrate on the radial component of the current density and consider the horizontal components in higher orders of the Taylor series.

The toroidal magnetic field $\underline{B}_T^{sh}$ is generated by poloidal currents $\underline{j}_P$ (cf. Eq. (11)). Ampère's law yields

$$\mu_0 \underline{j}_P = \partial_{\underline{x}} \times \underline{B}_T^{sh} = \partial_{\underline{x}} \times \left[\partial_{\underline{x}} \times \left(\underline{r}\Psi_T^{sh}\right)\right] \tag{46}$$

$$= \frac{1}{r\sin(\theta)}\left[-\partial_\theta\left(\sin(\theta)\partial_\theta \Psi_T^{sh}\right) - \frac{1}{\sin(\theta)}\partial_\lambda^2 \Psi_T^{sh}\right]\underline{e}_r \tag{47}$$

$$+ \frac{1}{r}\partial_\theta \partial_r\left(r\Psi_T^{sh}\right)\underline{e}_\theta + \frac{1}{r\sin(\theta)}\partial_\lambda \partial_r\left(r\Psi_T^{sh}\right)\underline{e}_\lambda. \tag{48}$$

The components of the horizontal $\underline{e}_\theta$- and $\underline{e}_\lambda$-direction are proportional to $\partial_r\left(r\Psi_T^{sh}\right)$. Therefore, the ansatz

$$a_l^m(r) = \frac{R_\mathrm{M}}{r}\left[a_l^m + a'^m_l \rho + \mathcal{O}(\rho^2)\right] \tag{49}$$

and

$$b_l^m(r) = \frac{R_\mathrm{M}}{r}\left[b_l^m + b'^m_l \rho + \mathcal{O}(\rho^2)\right], \tag{50}$$

where $\rho = \frac{r-b}{R_\mathrm{M}}$ and a_l^m, a'^m_l, b_l^m, b'^m_l are constants for each pair of l and m, is utilized. In the first order of the Taylor series expansion in the vicinity of the mean radius b, where $\Psi_T^{sh} \sim \frac{1}{r}$, the horizontal components of $\underline{j}_P$ vanish and only the contributions of the radial currents driving the toroidal magnetic field are considered (Olsen 1997). Using higher orders of the Taylor series, also the contributions of the horizontal components of $\underline{j}_P$ to the toroidal magnetic field in the vicinity of the mean radius b can be incorporated.

The scalar function of the toroidal magnetic field results in

$$\Psi_T^{sh} = \frac{R_\mathrm{M}}{r}\sum_{l=1}^{\infty}\sum_{m=0}^{l}\left[\alpha_l^m + \alpha'^m_l \rho + \mathcal{O}(\rho^2)\right]P_l^m(\cos(\theta)), \tag{51}$$

where $\alpha_l^m = a_l^m \cos(m\lambda) + b_l^m \sin(m\lambda)$ and $\alpha'^m_l = a'^m_l \cos(m\lambda) + b'^m_l \sin(m\lambda)$ (Olsen 1997). Thereby, each order of the Taylor series is linked with an additional set of expansion coefficients a_l^m, b_l^m, a'^m_l, b'^m_l and so on which can be reconstructed from the data in analogy to the Gauss coefficients.

From a mathematical point of view the scalar function Ψ_P^{sh} of the poloidal magnetic field $\underline{B}_P^{sh}$ can be parametrized analogously to the toroidal counterpart. But within the reconstruction procedure the poloidal fields that are generated by toroidal currents flowing inside the shell cannot be distinguished from the internally and externally driven poloidal fields, since these fields follow the same topological structure. But when the half thickness of the shell, defined by $h = (c-a)/2$ is smaller than the length scale on which the toroidal currents change in radial direction, the shell is called a thin shell and the scalar function Ψ_P^{sh} of the poloidal field $\underline{B}_P^{sh}$ vanishes within this thin shell approximation (Backus 1986; Backus et al. 1996) as illustrated in the following section.

The thin shell approximation

The thin shell approximation (Backus 1986; Backus et al. 1996) finally allows the separation of the poloidal field into its internal and external contributions.

Conferring to Eq. (6), the Mie representation for the magnetic field in the whole space $\mathbb{R}^3$ is given by

$$\underline{B} = \partial_{\underline{x}} \times (\Psi_T \underline{r}) + \partial_{\underline{x}} \times \left[\partial_{\underline{x}} \times (\Psi_P \underline{r})\right]. \tag{52}$$

Following Ampère's law the current density $\underline{j}$ is also solenoidal and can as well be parameterized via the Mie representation resulting in

$$\mu_0 \underline{j} = \partial_{\underline{x}} \times (\Gamma_T \underline{r}) + \partial_{\underline{x}} \times \left[\partial_{\underline{x}} \times (\Gamma_P \underline{r})\right] \tag{53}$$

with related scalar functions Γ_T and Γ_P.

Since the poloidal part of the current density corresponds with the curl of the toroidal magnetic field, the comparision of Eq. (53) with Eq. (9) shows that the scalar function Ψ_T and Γ_P are the same

$$\Psi_T = \Gamma_P. \tag{54}$$

Analogously, the toroidal part of the current density corresponds with the curl of the poloidal magnetic field and the comparision of Eq. (53) with Eq. (10) shows that the functions Ψ_P and Γ_T are related via

$$\partial_{\underline{x}}^2 \Psi_P = -\Gamma_T, \tag{55}$$

so that the function Ψ_P is given by the Green's function method

$$\Psi_P(\underline{r}) = \frac{1}{4\pi}\int_{\mathbb{R}^3} \frac{\Gamma_T(\underline{r}')}{|\underline{r} - \underline{r}'|}\,\mathrm{d}^3 r'. \tag{56}$$

Due to the underlying geometry the toroidal current density $\underline{j}_T$ flowing in the whole space can be written as the sum of the toroidal currents $\underline{j}_T^i$ flowing in the region $r < a$, the toroidal currents $\underline{j}_T^e$ flowing in the region $r > c$ and the toroidal currents $\underline{j}_T^{sh}$ flowing inside the spherical shell in the region $a \le r \le c$, so that

$$\underline{j}_T = \underline{j}_T^i + \underline{j}_T^e + \underline{j}_T^{sh}. \tag{57}$$

Thereby, the Mie representation of each part is given by

$$\underline{j}_T^i = \partial_{\underline{x}} \times \left(\Gamma_T^i \underline{r}\right) \tag{58}$$

$$\underline{j}_T^e = \partial_{\underline{x}} \times \left(\Gamma_T^e \underline{r}\right) \tag{59}$$

$$\underline{j}_T^{sh} = \partial_{\underline{x}} \times \left(\Gamma_T^{sh} \underline{r} \right) \tag{60}$$

with $\Gamma_T^i = \Gamma_T \, \chi_{[r<a]}$, $\Gamma_T^e = \Gamma_T \, \chi_{[r>c]}$ and $\Gamma_T^{sh} = \Gamma_T \, \chi_{[a<r<c]}$, where

$$\chi_I(x) = \begin{cases} 1 \ , x \in I \\ 0 \ , x \notin I \end{cases} \tag{61}$$

is the indicator function of the interval I. Using this segmentation the scalar function of the poloidal field can be rewritten as

$$\begin{aligned} \Psi_P(\underline{r}) = & \frac{1}{4\pi} \int_{V(r'<a)} \frac{\Gamma_T^i(\underline{r}')}{|\underline{r} - \underline{r}'|} \, \mathrm{d}^3 r' \\ & + \frac{1}{4\pi} \int_{V(r'>a)} \frac{\Gamma_T^e(\underline{r}')}{|\underline{r} - \underline{r}'|} \, \mathrm{d}^3 r' \\ & + \frac{1}{4\pi} \int_{S(a,c)} \frac{\Gamma_T^{sh}(\underline{r}')}{|\underline{r} - \underline{r}'|} \, \mathrm{d}^3 r'. \end{aligned} \tag{62}$$

Thus, the part of the scalar function that corresponds to the poloidal magnetic field which is generated inside the shell is given by

$$\Psi_P^{sh}(\underline{r}) = \frac{1}{4\pi} \int_{S(a,c)} \frac{\Gamma_T^{sh}(\underline{r}')}{|\underline{r} - \underline{r}'|} \, \mathrm{d}^3 r'. \tag{63}$$

Since $2b = a + c$ and $2h = c - a$ the bounds of integration can be rewritten as $a = b - h$ and $c = b + h$, so that

$$\Psi_P^{sh}(\underline{r}) = \frac{1}{4\pi} \int_{S(b-h,b+h)} \frac{\Gamma_T^{sh}(\underline{r}')}{|\underline{r} - \underline{r}'|} \, \mathrm{d}^3 r'. \tag{64}$$

Analogously to the scalar function Ψ_T, the function Γ_T can be expanded into a Taylor series in the vicinity of the mean radius b, resulting in

$$\Gamma_T^{sh}(\underline{r}') = \sum_{n=0}^{\infty} \frac{1}{n!} \partial_{r'}^n \Gamma_T^{sh} \big|_{r'=b} (r' - b)^n. \tag{65}$$

Substituting the Taylor series into the function Ψ_P^{sh} delivers

$$\Psi_P^{sh}(\underline{r}) = \frac{1}{4\pi} \sum_{n=0}^{\infty} \frac{1}{n!} \int_{S(b-h,b+h)} \partial_{r'}^n \Gamma_T^{sh} \big|_{r'=b} \frac{(r' - b)^n}{|\underline{r} - \underline{r}'|} \, \mathrm{d}^3 r'. \tag{66}$$

For the further evaluation of the integral it is assumed that the derivatives of the toroidal currents with respect to r are bounded, i.e., there exists a constant $L > 0$, so that

$$L^n \left| \partial_r^n \underline{j}_T \right| \leq \left| \underline{j}_T \right| \tag{67}$$

for $n \in \mathbb{N}$. Thus, L represents the length scale on which the toroidal currents change in radial direction. From

$$\begin{aligned} \underline{j}_T &= \partial_{\underline{x}} \times (\Gamma_T \underline{r}) \\ &= \frac{1}{\sin(\theta)} \partial_\lambda \Gamma_T \, \underline{e}_\theta - \partial_\theta \Gamma_T \, \underline{e}_\lambda \\ &= \left(\frac{1}{\sin(\theta)} \underline{e}_\theta \partial_\lambda - \underline{e}_\lambda \partial_\theta \right) \Gamma_T \end{aligned} \tag{68}$$

and therefore

$$\partial_r^n \underline{j}_T = \left(\frac{1}{\sin(\theta)} \underline{e}_\theta \partial_\lambda - \underline{e}_\lambda \partial_\theta \right) \partial_r^n \Gamma_T \tag{69}$$

it follows that

$$L^n \left| \partial_r^n \Gamma_T^{sh} \right| \leq \left| \Gamma_T^{sh} \right| \tag{70}$$

or equivalently

$$\left| \partial_r^n \Gamma_T^{sh} \right| \leq \frac{\left| \Gamma_T^{sh} \right|}{L^n}. \tag{71}$$

Since $r' \in [b - h, b + h]$, each summand within the Taylor series can be estimated upwards via

$$\left| \partial_{r'}^n \Gamma_T^{sh}(b) \right| \cdot \left| r' - b \right|^n \leq \frac{\left| \Gamma_T^{sh}(b) \right|}{L^n} \cdot h^n \tag{72}$$

delivering for Eq. (66)

$$\left| \Psi_P^{sh}(\underline{r}) \right| \leq \frac{1}{4\pi} \sum_{n=0}^{\infty} \frac{1}{n!} \left(\frac{h}{L} \right)^n \max_{\theta', \lambda'} \left\{ \left| \Gamma_T^{sh}(b) \right| \right\} \int_{S(b-h,b+h)} \frac{1}{|\underline{r} - \underline{r}'|} \, \mathrm{d}^3 r'. \tag{73}$$

The integral in Eq. (73) may be evaluated for any $\underline{r} \in \mathbb{R}^3$ but we restrict to $\underline{r}$ inside the shell as only there the magnetic field is measured. Then, the remaining integral results in

$$\int_{S(b-h,b+h)} \frac{1}{|\underline{r}-\underline{r}'|}\,\mathrm{d}^3 r' = \frac{4\pi}{3}\,\frac{1}{r}\left[r^3-(b-h)^3\right] + 2\pi\left[(b+h)^2-r^2\right], \tag{74}$$

utilizing that the coordinate system can be chosen properly so that θ' defines the angle between $\underline{r}$ and $\underline{r}'$. Therefore

$$|\Psi_P^{sh}(\underline{r})| \le \sum_{n=0}^{\infty} \frac{1}{n!}\left(\frac{h}{L}\right)^n \max_{\theta',\lambda'}\left\{|\Gamma_T^{sh}(b)|\right\}\left\{\frac{1}{3}\left[r^2-\frac{(b-h)^3}{r}\right]+\frac{1}{2}\left[(b+h)^2-r^2\right]\right\}. \tag{75}$$

For all $r \in [b-h, b+h]$, the function

$$f(r) = \frac{1}{3}\left[r^2-\frac{(b-h)^3}{r}\right]+\frac{1}{2}\left[(b+h)^2-r^2\right] \tag{76}$$

is non-negative and reaches its maximum value at $r = b-h$ with the related function value $f(b-h) = 2bh$. Therefore, an upper bound for Ψ_P^{sh} can finally be estimated as

$$\begin{aligned}\left|\Psi_P^{sh}(\underline{r})\right| &\le 2bh\sum_{n=0}^{\infty}\frac{1}{n!}\left(\frac{h}{L}\right)^n \max_{\theta',\lambda'}\left\{\left|\Gamma_T^{sh}(b)\right|\right\}\\ &= 2bL\sum_{n=0}^{\infty}\frac{1}{n!}\left(\frac{h}{L}\right)^{n+1} \max_{\theta',\lambda'}\left\{\left|\Gamma_T^{sh}(b)\right|\right\}.\end{aligned} \tag{77}$$

When $h \ll L$, the spherical shell is called a thin shell (Backus 1986; Backus et al. 1996) and the scalar function Ψ_P^{sh} of the poloidal magnetic field $\underline{B}_P^{sh}$ vanishes. The scalar function Ψ_T^{sh}, however, remains finite for all h as shown in Appendix A. Thus, if the shell may be regarded as thin, then the contribution of the toroidal currents in this shell to the poloidal magnetic field may be neglected. The poloidal magnetic field is mainly driven by currents beyond the shell. The contribution of the poloidal currents in this shell to the toroidal magnetic field may not be neglected.

From a first point of view the thin shell approximation is not an intuitive approximation. Considering the above presented nature of poloidal and toroidal magnetic fields it can be understood as follows:

The toroidal magnetic field only exists within current carrying regions (cf. Eq. 14) and thus, it is measurable only within these regions. Therefore, the spatial extent of the regions where the poloidal currents flow does not influence the strength of the toroidal magnetic field. It solely depends on the strength of the poloidal current density. In contrast to the toroidal magnetic field, the poloidal magnetic field is also measurable in current-free region. Thus, the poloidal field is a superposition of fields generated by currents flowing inside and outside the shell as well as currents flowing within the shell. This superposition is verified in Eq. (62). Therefore, the amount of the poloidal field generated by currents flowing within the shell has to be compared with the amount of the internal/external contributions. Furthermore, the poloidal field does not solely depend on the strength of the toroidal current density, since for the evaluation of the integrals also the volume where the current density flows is vital. Thus, a small toroidal current density that flows within a large volume outside/inside the shell can have a larger contribution to the field measured within the shell than a stronger current flowing within the thin shell.

Application of the thin shell approximation

The thin shell approximation is applied to parameterize the magnetic field in the vicinity of Mercury by the Gauss–Mie representation to reconstruct Mercury's internal magnetic field. The internal and external scalar potentials Φ^i and Φ^e are expanded into spherical harmonics up to third degree and order, representing the internal and external dipole, quadrupole and octupole fields. The scalar function Ψ_T^{sh} of the toroidal magnetic field $\underline{B}_T^{sh}$ is expanded into spherical harmonics up to second degree and order and additionally into a first order Taylor series for the radius. The scalar function Ψ_P^{sh} of the poloidal field $\underline{B}_P^{sh}$ is neglected within the thin shell approximation. Therefore, the total field is parameterized by 46 expansion coefficients, i.e. Gauss internal dipole (g_1^0, g_1^1, h_1^1), Gauss internal quadrupole (g_2^0, g_2^1, h_2^1, g_2^2, h_2^2), Gauss internal octupole (g_3^0, g_3^1, h_3^1, g_3^2, h_3^2, g_3^3, h_3^3), Gauss external dipole (q_1^0, q_1^1, s_1^1), Gauss external quadrupole (q_2^0, q_2^1, s_2^1, q_2^2, s_2^2), Gauss external octupole (q_3^0, q_3^1, s_3^1, q_3^2, s_3^2, q_3^3, s_3^3), toroidal coefficients (a_1^0, a_1^1, b_1^1, a_2^0, a_2^1, b_2^1, a_2^2, b_2^2, $a_1'^0$, $a_1'^1$, $b_1'^1$, $a_2'^0$, $a_2'^1$, $b_2'^1$, $a_2'^2$, $b_2'^2$). These 46 coefficients are estimated with Capon's method (Capon 1969; Toepfer et al. 2020a, b). The Capon method and the underlying model are tested against simulated data and MESSENGER in situ data around Mercury.

Hybrid simulation of Mercury's magnetosphere

For the first application of the thin shell approximation simulated magnetic field data are analyzed. The magnetic field resulting from the plasma interaction of Mercury with the solar wind is simulated with the hybrid code AIKEF (Müller et al. 2011), that has successfully been applied to several problems in Mercury's plasma interaction, (Exner et al. 2018, 2020, e.g.). The internal Gauss coefficients $g_1^0 = -190$ nT (dipole field), $g_2^0 = -78$ nT (quadrupole field) and $g_3^0 = -20$ nT (octupole field) (Anderson et al. 2012; Thébault et al. 2018; Wardinski et al. 2019) are implemented in the simulation code. The interplanetary magnetic field with a magnitude of $B_{\mathrm{IMF}} = 20$ nT is orientated along the vector $(x, y, z)^T = (0.0, 0.43, 0.9)^T$ in the MASO frame. The solar wind velocity of $v_{\mathrm{sw}} = 400$ km/s points along the x-axis (away from the Sun) and the solar wind proton density number was chosen to $n_{\mathrm{sw}} = 30\ \mathrm{cm}^{-3}$. The resulting magnitude of the magnetic field and the corresponding current density in the x-z-plane are displayed in Figs. 2, 3.

The internal dipole field dominates the geometry of Mercury's magnetosphere. Yet the quadrupole field in terms of the apparently shifted dipole field is visible. The influence of the octupole field is not clearly noticeable on the field lines in the figure. Furthermore, the distribution of the simulated current density shows that there exist no completely current-free region around Mercury.

Reconstruction of the Gauss coefficients from simulated data

For the reconstruction of the internal Gauss coefficients implemented in the simulation code, first of all, magnetic field data at a distance of $0.2\,R_{\mathrm{M}}$ from Mercury's surface are evaluated. The data are retrieved along meridional circular orbits around Mercury. The orbital plane is rotated about the rotation axis (z-axis) from -50° (afternoon/post-midnight sector) over 0° (noon/midnight, x-z-plane) to 50° (morning/pre-midnight sector). For this synthetically generated ideal case in terms of the thin shell approximation, the spherical shell that covers the circular orbits has a vanishing thickness $h = 0$ so that the application of the thin shell approximation is surely valid. The reconstructed internal Gauss coefficients are listed in Table 1. The optimal diagonal loading parameter which determines how the data are weighted within the application of Capon's method results in $\sigma_{opt.} \approx 1000$ nT (Toepfer et al. 2020b).

The deviation $\left|\underline{g}^{int} - \underline{g}_C^{int}\right|$ between the reconstructed internal coefficients $\underline{g}_C^{int}$ and the implemented internal coefficients $\underline{g}^{int}$ results in 4.0 nT, i.e. $\left|\underline{g}^{int} - \underline{g}_C^{int}\right| / \left|\underline{g}^{int}\right| \approx 1.9\%$ and thus, the implemented coefficients are reconstructed from the data with good precision.

Concerning the BepiColombo mission the generated circular orbits are idealized cases which are not realizable in practice. To investigate the applicability of the thin shell approximation for elliptical orbits we analyze the magnetic field data along the prospective orbits of MPO. The orbits are generated in analogy to the circular orbits, i.e., with the same longitudinal extend. Along this trajectories the distances of the data points from Mercury's surface vary from $0.12\,R_{\mathrm{M}}$ up to $0.6\,R_{\mathrm{M}}$ resulting in a shell thickness of $2h \approx 0.48\,R_{\mathrm{M}}$. Although the shell is now much thicker the thin shell approximation works successfully. The reconstructed Gauss coefficients are displayed in Table 2. The optimal diagonal loading parameter for the application of Capon's method results in $\sigma_{opt.} \approx 1000$ nT.

The deviation between the reconstructed and the implemented internal coefficients results in 4.1 nT, i.e. 1.9% and thus, these values agree with the coefficients reconstructed from the data evaluated along the circular orbits. Since the data are evaluated along the MPO orbits, it is expectable that also Mercury's internal octupole field will be reconstructed with good precision from the data of the magnetometer on board MPO.

It should be noted that the extension of the underlying model by the parameterization of the external parts of the field using the Gauss–Mie representation improves the results significantly. When only the internal parts

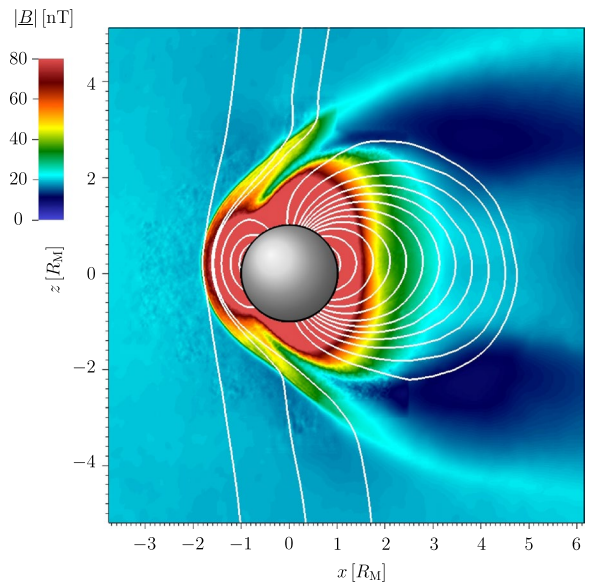

Fig. 2 Simulated magnitude of the magnetic field $\underline{B}$ in the x-z-plane. The white lines represent the magnetic field lines and the grey circle of radius 1 R_{M} symbolizes Mercury

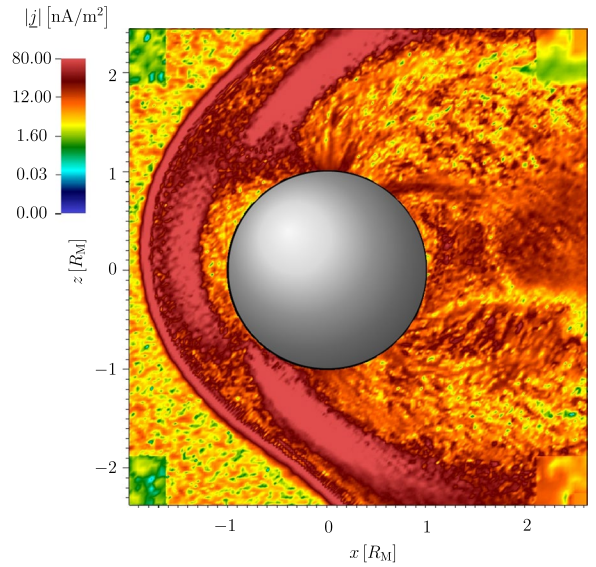

Fig. 3 Simulated magnitude of the current density $\underline{j}$ in the *x*-*z*-plane. The grey circle of radius 1 R_M symbolizes Mercury

of the field $\underline{B}^i$ are considered in the model, the deviation between the implemented and the reconstructed coefficients results in 29.7 nT or 14.4%, respectively (cf. Table 2). Additional parameterization of the external poloidal fields $\underline{B}^e$ using the external scalar potential Φ^e yields a deviation of 10.0 nT or 4.9%, respectively. Thus, for the analysis of Mercury's internal magnetic field, the Gauss–Mie representation is a suitable alternative to the application of global magnetospheric models.

Validity of the thin shell approximation

The coefficients reconstructed from the data evaluated along the planned *MPO trajectories* are basically in agreement with that from the data along the *circular orbits* although the shell covering the MPO orbits has a finite thickness.

To investigate the limits of the thin shell approximation within the hybrid simulation, the thickness of the shell is increased incrementally. Referring to Eq. (67), the length scale L is estimated via radial variation of the current distribution

$$L = \frac{|\underline{j}_H|}{|\partial_r \underline{j}_H|} \tag{78}$$

for the horizontal currents $\underline{j}_H = \underline{j} - \left(\underline{j} \cdot \underline{e}_r\right)\underline{e}_r$ which are used as a proxy for the toroidal currents at each point along the orbit. Since L represents a local quantity that varies for each point along the orbit, whereas the half thickness h is a global quantity, the set of resulting length scales is averaged over the number of points along the orbit resulting in the mean length scale $\langle L \rangle$. It should be noted that also the poloidal currents have horizontal components. Thus, the estimation of the length scale L with the horizontal currents $\underline{j}_H$ as a proxy for the toroidal currents is not exact, but it is sufficient for a qualitative discussion.

Table 1 Implemented and reconstructed Gauss coefficients for the dipole, quadrupole and octupole field resulting from the simulated data along the circular orbits at a distance of 0.2 R_M from Mercury's surface

Gauss coefficient	Input in nT	Output Capon in nT
g_1^0	− 190.0	− 191.2
g_1^1	0.0	− 1.9
h_1^1	0.0	− 1.7
g_2^0	− 78.0	− 76.0
g_2^1	0.0	1.3
h_2^1	0.0	− 0.5
g_2^2	0.0	− 0.5
h_2^2	0.0	− 0.2
g_3^0	− 20.0	− 20.3
g_3^1	0.0	0.5
h_3^1	0.0	0.4
g_3^2	0.0	− 0.1
h_3^2	0.0	0.9
g_3^3	0.0	1.0
h_3^3	0.0	− 0.2

The deviations between the ideal coefficients implemented in the simulation and the reconstructed coefficients for varying values of $h/\langle L \rangle$ are displayed in Table 3.

When h approaches $\langle L \rangle$ the deviations are greater than 12 nT. This deviation is of the same order when the parameterization is restricted to the Gauss representation. But for the data points along the MPO orbits, where $h/\langle L \rangle \approx 0.47$, the application of thin shell approximation is justified.

Since a shell of thickness $2h \approx 0.48\,R_M$ is called thin, the name *thin shell* is misleading, although this naming has been adopted within the literature. Conferring to the global length scale of 1 R_M the shell of thickness 0.48 R_M is not thin, but compared with the current length scale L it is. Therefore, the term *thin* has to be understood in a mathematical sense.

Table 2 Implemented and reconstructed Gauss coefficients for the dipole, quadrupole and octupole field resulting from the simulated data along the future MPO orbits. For comparision in the last columns the reconstructed Gauss coefficients resulting from the sole parameterization of the internal parts $\underline{B}^i$ (Gauss internal, 15 coefficients considered within the model) as well as the coefficients resulting from the parameterization of the internal $\underline{B}^i$ and external poloidal fields $\underline{B}^e$ (Gauss internal external, 30 coefficients considered within the model) are presented

Gauss coefficient	Input in nT	Output capon in nT		
		Gauss–Mie	Gauss internal	Gauss internal external
g_1^0	− 190.0	− 190.9	− 188.3	− 190.2
g_1^1	0.0	− 2.1	0.8	− 0.8
h_1^1	0.0	1.7	− 18.6	− 5.7
g_2^0	− 78.0	− 76.1	− 78.5	− 76.0
g_2^1	0.0	0.7	5.6	3.3
h_2^1	0.0	0.0	0.7	− 0.1
g_2^2	0.0	0.3	0.5	0.4
h_2^2	0.0	0.4	4.1	4.5
g_3^0	− 20.0	− 19.5	− 14.3	− 20.8
g_3^1	0.0	0.6	− 0.5	0.4
h_3^1	0.0	− 0.1	0.9	− 0.2
g_3^2	0.0	− 1.9	15.2	− 2.1
h_3^2	0.0	0.2	0.4	− 0.2
g_3^3	0.0	0.8	− 3.0	− 0.4
h_3^3	0.0	− 0.4	14.4	5.1
q_1^0	–	− 34.0	–	− 35.9
q_1^1	–	− 8.3	–	− 7.2
s_1^1	–	− 6.4	–	− 9.1

Table 3 Deviation between the implemented and the reconstructed Gauss coefficients for varying ratios of the half thickness h to the mean current length scale $\langle L \rangle$

h in R_M	$\langle L \rangle$ in R_M	$h/\langle L \rangle$	Devitation in nT	Devitation in %
0.24	0.51	0.47	4.1	1.9
0.32	0.49	0.65	4.8	2.3
0.43	0.46	0.94	12.8	6.2
0.62	0.42	1.5	13.5	7.0
1.09	0.37	2.9	16.8	8.1

Reconstruction of the Gauss coefficients from MESSENGER data

The Gauss–Mie representation has successfully been validated for the simulated data. For the reconstruction of the Gauss coefficients from the MESSENGER data only data points in the northern hemisphere within a distance of $r \leq 1.5\,R_M$ and $x > -0.4\,R_M$ from Mercury's surface can be considered because the orbits do not cover the southern hemisphere properly.

For the reconstruction of Mercury's internal magnetic field, the data from nine pairs of MESSENGER orbits with different orientations of the periapsis between 10. August 2012 and 14. July 2014 are analyzed. The combination of the orbits improves the model resolution compared to the analysis of single orbits. A discussion of the model resolution, as provided by Connerney (1981), can be found in the Appendix B. As a proof of concept, only a small subset of the whole MESSENGER data set is analyzed. In the case of a small and noisy data set the performance of the estimator can be improved by seperating the data set into several subsets (Meir 1994). Therefore, the Gauss coefficients are reconstructed for each pair of orbits and the results are averaged over the nine pairs. Outliers were not included within the averaging. The resulting mean values are listed in Table 4. The reconstructed coefficients for each pair of orbits and the standard deviations of the mean values are listed in Table 5 of Appendix C.

The mean values of the reconstructed internal Gauss coefficients and the external dipole coefficients are in feasible agreement with the values provided by Anderson et al. (2012), Thébault et al. (2018) and Wardinski et al. (2019). Furthermore, the related standard deviations for each coefficient are within the range of the variations resulting from the time varying magnetic field (Wardinski et al. 2019). To classify the coefficients reconstructed from the simulated magnetic field data (Table 2) in terms of that resulting from the MESSENGER data, the simulated data are furthermore evaluated along the MESSENGER trajectories. The reconstructed Gauss coefficients are listed in Table 6 of Appendix C. These coefficients are in agreement with the results presented in Table 4. Since the reconstructed coefficients resulting from the data evaluated along the MPO trajectories are in better agreement with the implemented coefficients than the coefficients resulting from the data evaluated along the MESSENGER trajectories, the restriction of the data points to the northern hemisphere and the related degradation of the model resolution influences the results significantly (Heyner et al. 2020, cf). Furthermore, it should be noted that the analysis of the length scales of the current densities (cf. "Validity of the thin shell approximation" section) cannot be performed for the MESSENGER orbits, because the current densities in the vicinity of the orbits are unknown.

Table 4 Gauss coefficients for the internal dipole, quadrupole and octupole field and for the external dipole field reconstructed from MESSENGER data. In the last colum the ranges of Gauss coefficients reconstructed from MESSENGER data by Anderson et al. (2012), Thébault et al. (2018) and Wardinski et al. (2019) are shown

Gauss coefficient	Output capon in nT	Ranges of former works in nT
g_1^0	– 175.9	– 215.8 to – 190.0
g_1^1	– 1.7	– 2.9 – 0.9
h_1^1	4.5	0.8 – 2.7
g_2^0	– 82.0	– 83.2 to – 57.7
g_2^1	0.8	– 1.5 – 3.4
h_2^1	1.0	– 1.4 – 0.0
g_2^2	2.9	– 7.0 to – 1.4
h_2^2	1.7	– 3.3 – 0.4
g_3^0	– 19.1	– 36.7 to – 15.7
g_3^1	1.1	1.8 – 4.1
h_3^1	0.4	0.3 – 0.8
g_3^2	– 0.5	– 1.5 – 9.2
h_3^2	– 5.9	0.9 – 2.6
g_3^3	– 5.8	– 2.5 to– 1.4
h_3^3	– 3.3	0.1 – 0.3
q_1^0	– 36.6	– 39.7 to – 23.2
q_1^1	– 7.4	– 0.2 – 0.7
s_1^1	0.8	– 0.1 – 1.5

Summary and outlook

In the vicinity of Mercury no completely current-free region is present. Therefore, the Gauss representation does not yield a proper parametrization of Mercury's magnetospheric field. Extension of the Gauss representation to the Gauss–Mie representation allows a more complete characterization of Mercury's internal and magnetospheric field.

For the parameterization of the magnetic field the orbit where the magnetic field is measured, is conceptually covered by a spherical shell. Due to the underlying geometry the total measured magnetic field is a superposition of internal and external poloidal fields generated by toroidal currents flowing outside the spherical shell as well as toroidal and poloidal fields generated by currents flowing within the shell. Thereby, each component of the field is either described by a scalar potential (Φ^i, Φ^e) or a scalar function (Ψ_P^{sh}, Ψ_T^{sh}). These potentials and functions can be expanded into spherical harmonics. When the thickness of the spherical shell is smaller than the length scale on which the toroidal current density changes in radial direction the shell is called a thin shell. Then the poloidal field generated by currents flowing inside the shell is negligible compared to the poloidal field generated by currents flowing beyond the shell, whereas the toroidal field remains finite. In the case of the planned MPO orbits, the thin shell approximation is a reasonable choice.

For the application of the thin shell approximation the internal Gauss coefficients for the dipole, quadrupole and octupole field are implemented in the simulation code AIKEF and the magnetic field data resulting from the plasma interaction of Mercury with the solar wind are simulated in the vicinity of Mercury. The data are evaluated along the planned MPO orbits and the 46 expansion coefficients, describing the internal, external and the toroidal field are reconstructed with Capon's method. Since the reconstructed internal Gauss coefficients are in good agreement with that implemented in the simulation code, the parameterization of the magnetic field using the Gauss–Mie representation is a suitable alternative to the application of global magnetospheric models. Even the implemented Gauss coefficient for the octupole field of Mercury can be reconstructed accurately and therefore, it is expectable that Mercury's internal octupole field will be reconstructed with high precision from the magnetometer data on board MPO. Thus, it is worthwile to investigate the analysis of higher multipoles, such as hexadecapole, from the data along the MPO trajectories.

Furthermore, the thin shell approximation is applied to reconstruct Mercury's internal magnetic field from the data of the MESSENGER mission. The results are in reasonable agreement with former works. Since only the data points in the northern hemisphere are vital for the analysis of the MESSENGER data, the symmetrically distributed MPO orbits will deliver a better model resolution than the MESSENGER orbits.

Concerning the BepiColombo mission the combination of the Gauss representation with the Mie representation is a useful model for the analysis of Mercury's internal magnetic field. As the BepiColombo mission consits of two elements, the planetary orbiter and the magnetospheric orbiter, measurements of any gradients of Mercury's magnetic field are possible which may lead to further improvements of the methods presented here. Besides the analysis of the internal magnetic field, the reconstructed coefficients for the toroidal magnetic field can be used for calculating poloidal current systems, e.g. field aligned currents, in the vicinity of the orbit where the data are evaluated.

Appendix A: The thin shell approximation for the toroidal magnetic field

As derived in "The thin shell approximation" section, the scalar function of the poloidal magnetic field can be estimated upwards as

$$\left|\Psi_P^{sh}(\underline{r})\right| \leq 2bL \sum_{n=0}^{\infty} \frac{1}{n!} \left(\frac{h}{L}\right)^{n+1} \max_{\theta',\lambda'} \left\{\left|\Gamma_T^{sh}(b)\right|\right\}. \tag{79}$$

When $h \ll L$, the function Ψ_P^{sh} vanishes. Now the influence of the thin shell approximation for the toroidal magnetic field $\underline{B}_T^{sh}$ is discussed.

The scalar function Ψ_T^{sh} of the toroidal magnetic field $\underline{B}_T^{sh}$ can be expanded analogously into a Taylor series in the vicinity of the mean radius b

$$\Psi_T^{sh}(\underline{r}) = \Gamma_P^{sh}(\underline{r}) = \sum_{n=0}^{\infty} \frac{1}{n!} \partial_r^n \Gamma_P^{sh}(r)\big|_{r=b} (r-b)^n, \tag{80}$$

using that the scalar functions Ψ_T^{sh} and Γ_P^{sh} are the same (cf. Eq. 54).

If we furthermore assume that also the radial derivatives of the poloidal current density are bounded so that

$$\left|\partial_r^n \Gamma_P^{sh}\right| \leq \frac{\left|\Gamma_P^{sh}\right|}{L^n}, \tag{81}$$

the function $\Psi_T^{sh}(\underline{r})$ can be estimated upwards as

$$\begin{aligned} |\Psi_T^{sh}(\underline{r})| &\leq \sum_{n=0}^{\infty} \frac{1}{n!} |\partial_r^n \Gamma_P^{sh}(b)| \cdot |r-b|^n \\ &\leq \sum_{n=0}^{\infty} \frac{1}{n!} \frac{|\Gamma_P^{sh}(b)|}{L^n} |r-b|^n. \end{aligned} \tag{82}$$

Using that $\Psi_T^{sh}(\underline{r})$ is solely evaluated within the spherical shell, where $r \in [b-h, b+h]$ and therefore $\left|r-b\right| \leq h$ results in

$$\left|\Psi_T^{sh}(\underline{r})\right| \leq \sum_{n=0}^{\infty} \frac{1}{n!} \left(\frac{h}{L}\right)^n \left|\Gamma_P^{sh}(b)\right|. \tag{83}$$

When $h \ll L$, the function Ψ_T^{sh} remains finite.

Appendix B: Model resolution

For the analysis of Mercury's internal magnetic field from the MESSENGER data only data points in the northern hemisphere can be considered. This limitation impairs the condition number κ of the shape matrix $\underline{\underline{H}}$ from $\kappa \approx 226$ for the data points along the MPO orbits to $\kappa \approx 10^8$ for the data points along a single MESSENGER orbit, where the shape matrix describes the spacial distribution of the data points. The condition number is defined as the ratio of the largest and the smallest singular value of the shape matrix. Therefore, some of the 46 singular values, corresponding to the 46 expansion coefficients, of the shape matrix have to be dropped within the numerical calculation to improve the condition number. Within the low rank approximation (Eckart and Young 1936) only k singular values, where $k \leq 46$, can be considered and therefore, the shape matrix $\underline{\underline{H}}$ is approximated by a shape matrix $\underline{\underline{H}}_k$ which has a lower rank and a lower condition number.

Capon's filter matrix

$$\underline{\underline{w}}^{\dagger} = \left[\underline{\underline{H}}^{\dagger} \underline{\underline{M}}^{-1} \underline{\underline{H}}\right]^{-1} \underline{\underline{H}}^{\dagger} \underline{\underline{M}}^{-1} \tag{84}$$

which is the key parameter for calculating Capon's estimator

$$\underline{g}_C = \underline{\underline{w}}^{\dagger} \underline{B} \tag{85}$$

fulfills the distortionless constraint

$$\underline{\underline{w}}^{\dagger} \underline{\underline{H}} = \underline{\underline{I}}, \tag{86}$$

where $\underline{\underline{I}}$ is the identity matrix and $\underline{\underline{M}} = \langle \underline{B} \circ \underline{B} \rangle$ describes the data covariance matrix of the magnetic field measurements $\underline{B}$ (Toepfer et al. 2020a, b). As a consequence of the low rank approximation Capon's filter matrix is modified to

$$\underline{\underline{w}}_k^{\dagger} = \left[\underline{\underline{H}}_k^{\dagger} \underline{\underline{M}}^{-1} \underline{\underline{H}}_k\right]^{-1} \underline{\underline{H}}_k^{\dagger} \underline{\underline{M}}^{-1} \tag{87}$$

so that

$$\underline{\underline{R}} = \underline{\underline{w}}_k^{\dagger} \underline{\underline{H}} \neq \underline{\underline{I}}. \tag{88}$$

The matrix $\underline{\underline{R}} = \underline{\underline{w}}_k^{\dagger} \underline{\underline{H}}$ is called the model resolution matrix. Because of

$$\underline{g}_C^k = \underline{\underline{R}}\, \underline{g}, \tag{89}$$

where $\underline{g}_C^k$ denotes the estimator resulting from the consideration of k singular values and $\underline{g}$ is the ideal coefficient vector implemented in the simulation code, the diagonal elements of $\underline{\underline{R}}$ identify the resolution of each coefficient (Connerney 1981). When $\underline{\underline{R}} = \underline{\underline{I}}$ each coefficient is resolved for 100%. If the resolution is smaller than 100%, there exist model parameter covariances.

The more singular values are considered within the estimation, the better the model resolution becomes, whereas the condition number of the shape matrix increases and thus, the influence of measurement errors increases.

To achieve a compromise between the resolution and the condition number, the coefficients are estimated

for different numbers of singular values and the change of the coefficients resulting from k singular values to the coefficients resulting from $k-1$ singular values is regarded. For the final computation the maximum number of singular values is chosen from which the reconstructed coefficients are almost constant. In Fig. 4 the procedure is exemplarily illustrated for the coefficient g_1^0, which corresponds to the diagonal element R_{11} by analyzing the data of one pair of MESSENGER orbits.

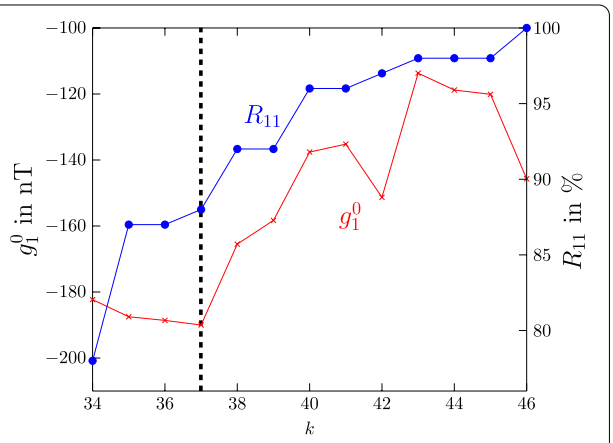

Fig. 4 Variation of the reconstructed coefficient g_1^0 (red) and the related model resolution R_{11} (blue) with respect to the number k of singular values. For $k \leq 37$ (dashed line) the reconstructed values of g_1^0 are almost constant

Changing the number of considered singular values incrementally from 46 to 37 the resulting coefficient changes significantly. For $k \leq 37$ the values are almost constant and therefore, 37 singular values, corresponding to a model resolution of 88% for the coefficient g_1^0 are considered within the estimation.

Appendix C: Tables: Reconstructed Gauss coefficients from MESSENGER orbits

Table 5 Gauss coefficients for the dipole, quadrupole and octupole field reconstructed from selected pairs of MESSENGER orbits

Orbits	g_1^0	g_1^1	h_1^1	g_2^0	g_2^1	h_2^1	g_2^2	h_2^2	g_3^0	g_3^1	h_3^1	g_3^2	h_3^2	g_3^3	h_3^3	q_1^0	q_1^1	s_1^1
2013–T245, 2014–T21	− 197.4	2.0	− 2.0	− 71.6	− 10.1	21.1	− 40.1	− 8.5	− 6.7	9.0	1.7	9.5	− 7.3	23.5	80.2	− 65.2	− 47.8	− 13.7
2014–T143, 2014–T195	− 190.0	18.0	15.3	− 66.7	16.9	− 7.6	5.2	2.7	− 11.5	− 10.9	− 24.5	4.0	− 11.4	− 43.4	− 21.9	− 24.2	− 12.1	− 21.9
2013–T330, 2014–T107	− 158.5	− 15.1	− 1.6	− 96.6	17.0	− 2.2	− 6.4	2.1	− 10.0	− 1.8	12.5	− 6.4	− 8.2	3.8	7.1	5.6	2.7	3.3
2013–T330, 2014–T195	− 164.1	− 6.5	6.6	− 81.2	12.7	6.3	12.0	− 52.2	− 13.6	− 5.9	− 14.1	− 6.3	3.6	− 32.5	21.5	− 5.8	− 16.2	14.3
2014–T107, 2014–T143	− 155.6	− 2.6	5.0	− 81.7	22.8	− 8.0	13.5	30.7	− 20.8	− 8.9	− 3.6	− 20.3	− 18.8	− 32.1	− 19.9	− 24.5	− 0.8	16.8
2012–T223, 2012–T311	− 190.4	0.2	0.5	− 76.0	73.0	11.9	− 30.0	− 82.1	− 17.4	− 65.6	− 68.5	− 41.4	88.9	− 178.1	53.2	9.6	41.1	− 41.5
2013–T330, 2014–T21	− 163.3	− 9.0	7.9	− 80.6	− 8.5	5.6	− 9.8	− 27.2	− 1.8	3.5	− 11.5	14.4	− 39.1	− 22.6	35.5	11.4	− 27.4	− 5.5
2014–T107, 2013–T245	− 162.3	− 4.7	− 27.2	− 96.6	− 9.5	16.0	− 29.6	32.0	− 27.5	10.7	31.2	− 21.7	− 13.2	25.1	35.5	− 61.5	− 1.7	− 38.4
2014–T195	− 163.7	8.7	− 17.3	− 87.0	− 12.8	− 21.2	− 22.1	10.5	− 32.9	12.8	17.3	− 18.4	13.7	53.2	− 41.4	− 38.2	− 16.2	12.3
Mean value	− 175.9	− 1.7	4.5	− 82.0	0.8	1.0	2.9	1.7	− 19.1	1.1	0.4	− 0.5	− 5.9	− 5.8	− 3.3	− 36.6	− 7.4	0.8
Standard deviation	15.8	5.9	6.2	10.2	13.9	8.2	10.6	7.8	8.5	9.2	12.7	12.1	11.0	26.8	21.2	23.2	8.4	15.0

Table 6 Gauss coefficients for the dipole, quadrupole and octupole field reconstructed from the simulated data evaluated at selected pairs of MESSENGER orbits

Orbits	g_1^0	g_1^1	h_1^1	g_2^0	g_2^1	h_2^1	g_2^2	h_2^2	g_3^0	g_3^1	h_3^1	g_3^2	h_3^2	g_3^3	h_3^3	q_1^0	q_1^1	s_1^1
2013–T245, 2014–T21	− 136.4	9.9	3.7	− 103.8	− 16.0	5.2	− 16.3	− 4.0	− 24.4	7.6	− 6.8	− 5.7	− 5.1	10.6	10.6	− 39.2	− 13.0	− 11.1
2014–T143, 2014–T195	− 179.6	− 10.5	− 4.4	− 93.7	21.6	7.4	− 3.6	− 15.0	− 12.2	− 10.7	− 10.9	3.7	5.7	− 13.9	2.1	− 31.9	− 27.5	4.3
2013–T330, 2014–T107	− 148.9	− 15.1	5.6	− 105.7	15.4	7.6	3.7	− 34.3	− 15.2	− 5.8	− 8.4	− 6.1	6.9	− 17.1	11.7	− 20.2	− 22.8	− 5.9
2013–T330, 2014–T195	− 149.3	− 12.6	3.7	− 99.4	10.4	4.1	7.0	− 31.0	− 18.2	− 3.5	− 4.1	− 6.8	2.3	− 16.9	17.0	− 12.8	− 18.7	− 6.8
2014–T107, 2014–T143	− 190.4	− 21.2	− 8.6	− 97.0	25.1	6.4	− 15.8	− 17.3	− 8.1	− 11.3	− 10.0	12.3	7.4	− 10.0	13.1	− 43.2	− 36.7	− 2.5
2012–T223, 2012–T311	− 150.1	16.3	− 1.8	− 113.9	27.9	2.7	24.8	− 39.4	− 28.8	− 44.8	− 4.4	− 57.4	77.5	− 79.4	− 16.4	− 41.5	− 9.8	− 35.4
2013–T330, 2014–T21	− 105.0	− 14.8	7.5	− 131.5	6.4	2.1	3.1	− 17.1	− 13.9	− 1.6	0.0	− 17.1	− 3.2	− 8.5	9.0	− 6.6	− 7.8	− 22.6
2014–T107, 2013–T245	− 144.5	− 28.4	1.6	− 117.6	36.5	21.9	1.7	− 10.5	− 8.7	− 13.7	− 18.8	− 5.7	2.3	− 25.1	6.6	− 4.6	− 37.9	6.8
2014–T195	− 131.5	6.8	− 6.3	− 114.8	− 51.6	− 11.7	− 1.9	0.4	− 19.0	46.0	− 9.7	− 0.1	− 41.7	82.1	− 7.4	− 53.3	− 3.4	51.7
Mean value	− 163.7	1.1	0.1	− 104.0	7.6	5.1	1.7	− 10.6	− 18.8	− 5.6	− 6.8	− 3.5	2.3	− 9.3	6.5	− 31.5	− 14.7	− 2.5
Standard deviation	19.9	14.0	5.6	8.1	14.3	2.2	3.9	7.4	5.9	7.3	3.7	4.3	4.9	10.4	7.1	12.4	8.6	6.9

Acknowledgements
The authors are grateful for stimulating discussions and helpful suggestions by Alexander Schwenke and the technial support by Willi Exner.

Authors' contributions
All authors contributed conception and design of the study; ST and UM wrote the first draft of the manuscript; all authors contributed to manuscript revision. All authors read and approved the final manuscript.

Funding
Open Access funding enabled and organized by Projekt DEAL. We acknowledge support by the German Research Foundation and the Open Access Publication Funds of the Technische Universität Braunschweig. The work by Y. Narita is supported by the Austrian Space Applications Programme at the Austrian Research Promotion Agency under contract 865967. D. Heyner and K.-H. Glassmeier were supported by the German Ministerium für Wirtschaft und Energie and the German Zentrum für Luft- und Raumfahrt under contract 50 QW1501.

Availability of data and materials
Simulation data can be provided upon request.

Declarations

Competing interests
The authors declare that they have no conflict of interest.

Author details
[1] Institut für Theoretische Physik, Technische Universität Braunschweig, Mendelssohnstraße 3, 38106 Braunschweig, Germany. [2] Space Research Institute, Austrian Academy of Sciences, Schmiedlstraße 6, 8042 Graz, Austria. [3] Institut für Geophysik und extraterrestrische Physik, Technische Universität Braunschweig, Mendelssohnstraße 3, 38106 Braunschweig, Germany. [4] Deutsches Zentrum für Luft- und Raumfahrt, Institut für Planetenforschung, Rutherfordstraße 2, 12489 Berlin, Germany. [5] Laboratoire de Planétologie et Géodynamique, UMR 6112, CNRS, Université de Nantes, Université d'Angers, 2 Rue de la Houssinière, 44000 Nantes, France.

Received: 18 December 2020 Accepted: 20 February 2021
Published online: 08 March 2021

References

Alexeev II, Belenkaya ES, Bobrovnikov SYu, Slavin JA, Sarantos M (2008) Paraboloid model of Mercury's magnetosphere. J Geophys Res. 113:A12210. https://doi.org/10.1029/2008JA013368
Alexeev II, Belenkaya ES, Slavin JA, Korth H, Anderson BJ, Baker DN, Boardsen SA, Johnson CL, Purucker ME, Sarantos M, Solomon SC (2010) Mercury's magnetospheric magnetic field after the first two MESSENGER flybys. Icarus 209:23–39. https://doi.org/10.1016/j.icarus.2010.01.024
Anderson BJ, Johnson CL, Korth H, Purucker ME, Winslow RM, Slavin JA, Solomon SC, McNutt RL Jr, Raines JM, Zurbuchen TH (2011) The global magnetic field of Mercury from MESSENGER orbital observations. Science 333:1859–1862. https://doi.org/10.1126/science.1211001
Anderson BJ, Johnson CL, Korth H, Winslow RM, Borovsky JE, Purucker ME et al (2012) Low-degree structure in Mercury's planetary magnetic field. J Geophys Res. 117:E00L12. https://doi.org/10.1029/2012JE004159
Backus G (1986) Poloidal and toroidal fields in geomagnetic field modeling. Rev Geophys. 24:75–109. https://doi.org/10.1029/RG024i001p00075
Backus G, Parker R, Constable C (1996) Foundations of Geomagnetism. Cambridge University Press, Cambridge
Bayer M, Freeden W, Maier T (2001) A vector wavelet approach to iono- and magnetospheric geomagnetic satellite data. J Atmos Solar-Terrestr Phys. 63:581–597. https://doi.org/10.1016/S1364-6826(00)00234-0
Benkhoff J, van Casteren J, Hayakawa H, Fujimoto M, Laakso H, Novara M, Ferri P, Middleton HR, Ziethe R (2010) BepiColombo-comprehensive exploration of mercury: mission overview and science goals. Planet Space Sci. 85(1–2):2–20. https://doi.org/10.1016/j.pss.2009.09.020
Capon J (1969) High resolution frequency-wavenumber spectrum analysis. Proc IEEE 57:1408–1418. https://doi.org/10.1109/PROC.1969.7278
Connerney JEP (1981) The magnetic field of Jupiter: a generalized inverse approach. J Geophys Res. 86:7679–7693. https://doi.org/10.1029/JA086iA09p07679
Eckart C, Young G (1936) The approximation of one matrix by another of lower rank. Psychometrika 1:211–218. https://doi.org/10.1007/BF02288367
Engels U, Olsen N (1999) Computation of magnetic fields within source regions of ionospheric and magnetospheric currents. J Atmos Solar-Terrestr Phys. 60:1585–1592. https://doi.org/10.1016/S1364-6826(98)00094-7
Exner W, Heyner D, Liuzzo L, Motschmann U, Shiota D, Kusano K, Shibayama T (2018) Coronal mass ejection hits mercury: A.I.K.E.F. hybrid-code results compared to MESSENGER data. Planet Space Sci 153:89–99. https://doi.org/10.1016/j.pss.2017.12.016
Exner W, Simon S, Heyner D, Motschmann U (2020) Influence of Mercury's exosphere on the structure of the magnetosphere. J Geophys Res. 125:e27691. https://doi.org/10.1029/2019JA027691
Gauß CF (1839) Allgemeine Theorie des Erdmagnetismus: Resultate aus den Beobachtungen des magnetischen Vereins im Jahre 1838, edited by: Gauss, C. F. and Weber, W., 1–57, Weidmannsche Buchhandlung, Leipzig, 1839
Glassmeier K-H, Motschmann U, Dunlop M, Balogh A, Acuña MH, Carr C, Musmann G, Fornaçon K-H, Schweda K, Vogt J, Georgescu E, Buchert S (2001) Cluster as a wave telescope-first results from the fluxgate magnetometer. Ann Geophys. 19:1439–1447. https://doi.org/10.5194/angeo-19-1439-2001
Glassmeier K-H, Auster H-U, Heyner D, Okrafka K, Carr C, Berghofer G, Anderson BJ et al (2010) The fluxgate magnetometer of the BepiColombo Mercury Planetary Orbiter. Planet Space Sci. 58:287–299. https://doi.org/10.1016/j.pss.2008.06.018
Glassmeier K-H, Tsurutani BT (2014) Carl friedrich gauss-general theory of terrestrial magnetism-a revised translation of the German text. Hist Geo Space Sci. 5:11–62. https://doi.org/10.5194/hgss-5-11-2014
Heyner D, Auster H-U, Fornacon K-H, Carr C, Richter I, Mieth JZD, Kolhey P et al (2020) The BepiColombo planetary magnetometer MPO-MAG: What can we learn from the Hermean magnetic field? Space Sci Rev.
Jacobs JA (1987) Geomagnetism 2. Press Acad, London
Johnson CL, Purucker ME, Korth H, Anderson BJ, Winslow RM, Al Asad MMH, Slavin JA, Alexeev II, Phillips RJ, Zuber MT, Solomon SC (2012) Messenger observations of Mercury's magnetic field structure. J Geophys Res. 117:0014. https://doi.org/10.1029/2012JE004217
Kazantsev SG, Kardakov VB (2019) Poloidal-toroidal decomposition of solenoidal vector fields in the ball. J Applied Industr Math. 13:480–499. https://doi.org/10.1134/S1990478919030098
Korth H, Anderson BJ, Acuña Mario H, Slavin JA, Tsyganenko NA, Solomon SC, McNutt RL (2004) Determination of the properties of Mercury's magnetic field by the messenger mission. Planet Space Sci. 52:733–746. https://doi.org/10.1016/j.pss.2003.12.008
Kosik JC (1984) Quantitative magnetospheric magnetic field modelling with toroidal and poloidal vector fields. Planet Space Sci. 32:965–974. https://doi.org/10.1016/0032-0633(84)90053-9
Krause F, Rädler K-H (1980) Mean-field magnetohydrodynamics and dynamo theory. Pergamon Press, Oxford
Mayer C, Maier T (2006) Separating inner and outer Earth's magnetic field from CHAMP satellite measurements by means of vector scaling functions and wavelets. Geophys J Int 167(3):1188–1203. https://doi.org/10.1111/j.1365-246X.2006.03199.x
Meir R (1994) Bias, variance and the combination of least squares estimators, MIT Press, Cambridge, MA, USA, Proceedings of the 7th International Conference on Neural Information Processing Systems, 295–302
Motschmann U, Woodward TI, Glassmeier K-H, Southwood DJ, Pinçon J-L (1996) Wavelength and direction filtering by magnetic measurements at satellite arrays: generalized minimum variance analysis. J Geophys Res. 101:4961–4966. https://doi.org/10.1029/95JA03471
Müller J, Simon S, Motschmann U, Schüle J, Glassmeier K-H, Pringle GJ (2011) A.I.K.E.F.: Adaptive hybrid model for space plasma simulations. Comp Phys Comm 182:946–966. https://doi.org/10.1016/j.cpc.2010.12.033
Narita Y, Glassmeier K-H, Treumann RA (2006) Wave-number spectra and intermittency in the terrestrial Foreshock region. Phys Rev Lett. 97:191101. https://doi.org/10.1103/PhysRevLett.97.191101
Narita Y (2012) Plasma Turbulence in the Solar System. Springer-Verlag, Berlin Heidelberg. https://doi.org/10.1007/978-3-642-25667-7

Olsen N (1997) Ionospheric F currents at middle and low latitudes estimated from Magsat data. J Geophys Res. 102:4569–4576. https://doi.org/10.1029/96JA02949
Olsen N, Glassmeier K-H, Jia X (2010) Separation of the magnetic field into external and internal parts. Space Sci Rev 152:135–157. https://doi.org/10.1007/s11214-009-9563-0
Thébault E, Langlais B, Oliveira JS, Amit H, Leclercq L (2018) A time-averaged regional model of the Hermean magnetic field. Phys Earth Planet Interior 276:93–105. https://doi.org/10.1016/j.pepi.2017.07.001
Toepfer S, Narita Y, Heyner D, Motschmann U (2020a) The Capon method for Mercury's magnetic field analysis. Front Phys. 8:249. https://doi.org/10.3389/fphy.2020.00249
Toepfer S, Narita Y, Heyner D, Kolhey P, Motschmann U (2020b) Mathematical foundation of Capon's method for planetary magnetic field analysis. Geosci Instrum Method Data Syst. 9:471–481. https://doi.org/10.5194/gi-9-471-2020
Wardinski I, Langlais B, Thébault E (2019) Correlated time-varying magnetic field and the core size of Mercury. J Geophys Res. 124:2178–2197. https://doi.org/10.1029/2018JE005835
Zharkova AY, Kreslavsky MA, Head JW, Kokhanov AA (2020) Regolith textures on Mercury: comparison with the Moon. Icarus 351:113945. https://doi.org/10.1016/j.icarus.2020.113945

Publisher's Note